Available online at www.sciencedirect.com
ScienceDirect
Trans. Nonferrous Met. Soc. China 32(2022) 192−205
Transactions of Nonferrous Metals Society of China
www.tnmsc.cn

Standard heat treatment effects on TLP bonded IN-738LC superalloy using BNi-9 filler: An approach to make an ideal joint

Danesh AMIRI, Ata KAMYABI-GOL, Seyed Abdolkarim SAJJADI

Department of Materials Science and Engineering, Engineering Faculty, Ferdowsi University of Mashhad, Mashhad, Iran

Received 14 December 2020; accepted 10 September 2021

Abstract: The present research is focused on the effects of standard heat treatment on the microstructure and mechanical properties of diffusion brazed IN-738LC superalloy. Three distinct heat treatment cycles of full solution annealing, partial solution annealing, and aging treatment were applied to the bonded specimens, sequentially. The results reveal that bonding at 1120 °C for 5 min leads to incomplete isothermal solidification and formation of eutectic phases including Ni- and Cr-rich borides in the joint centerline. Increasing the holding time to 45 min leads to the full isothermal solidification and formation of a nickel proeutectic solid-solution phase (γ) in the joints. The standard heat treatment of isothermally solidified and non-isothermally solidified specimens results in the complete elimination of the boride phases in the diffusion-affected zone and also the formation of γ' precipitates in the isothermally solidified zone. However, discontinuously re-solidified products are observed in joint district in the non-isothermally solidified sample. The highest shear strength (~801 MPa) is achieved for isothermally solidified specimen after standard heat treatment; this strength is approximately 99% that of the substrate material.

Key words: IN738LC; standard heat treatment; diffusion brazing; isothermal solidification; γ' precipitates; mechanical properties

1 Introduction

The nickel-based superalloys with high-temperature strength (~1 GPa), high-temperature corrosion and creep resistance are of great importance for high-temperature applications. The strength of these alloys mainly comes from multiple mechanisms, including solid solution strengthening, precipitation hardening and grain boundary strengthening [1,2]. However, IN-738LC faces numerous challenges in terms of weldability because of considerable amounts of Al and Ti (more than 6 wt.%) in its composition [3,4]. Segregation of Al and Ti in IN-738LC along with non-equilibrium phase transformations during non-equilibrium solidification in welding results in the formation of heat affected zone (HAZ) intergranular liquation cracking, which in turn leads to a reduction in the mechanical properties of the joint [5,6]. It is well established that HAZ liquation cracking is influenced by low melting point phases which occur during welding and post-weld heat treatment (PWHT) such as gamma prime precipitates, carbides and borides, γ-γ' eutectics and topologically close-packed phases (TCP) along the grain boundaries [7,8]. On the other hand, brazing of superalloys cannot avoid the formation of low melting point phases such as borides, silicides, and phosphides during this process [9,10].

To prevent the formation of detrimental intermetallic phases in the joints, transient liquid phase (TLP) bonding was developed as a superior technique to join/repair superalloys [11]. This

Corresponding author: Seyed Abdolkarim SAJJADI, Tel/Fax: +98-51-38805610, E-mail: sajjadi@um.ac.ir
DOI: 10.1016/S1003-6326(21)65787-4

method is based on diffusion of melting point depressant (MPD) elements such as silicon, boron and phosphorus from the filler metal to the substrate material (SM). The TLP bonding is performed at a temperature between the liquidus and the solidus of the filler metal and SM, respectively. During holding at bonding temperature, interdiffusion of alloying elements occurs between the substrate metal and the liquid filler metal. TLP bonding progresses through isothermal solidification of the liquid phase initiating from the base metal/bond region interface towards the center of the joint [12,13].

A complete isothermal solidification results in a single phase region without intermetallic phases in the joint centerline while the in-situ widespread boride precipitates are still observed in the diffusion affected zone (DAZ) [14,15]. These borides are formed by solid state diffusion of B into the substrate material during isothermal solidification and can drastically reduce the mechanical properties of the superalloy joint [16,17].

Post bond heat treatment (PBHT) is performed on joined/repaired components to eliminate DAZ precipitates and form a microstructure similar to the substrate material. POURANVARI et al [18] have reported that PBHT at 1150 °C for 12 h in TLP bonded IN718 components leads to a boride-free joint with a uniform chemical composition. According to a study carried out by WANG et al [19], the size and squareness of primary γ' increase dramatically while the volume fraction of the phase decreases in γ'-strengthened Co-based superalloy TLP-bonded using a Ni−Cr−W−B filler alloy. Generally speaking, a suitable PBHT should: (1) eliminate the boride phases in the DAZ, (2) homogenize the bond region in terms of chemical composition and (3) form γ' precipitates in the joint region similar to the substrate material. A proper PBHT should lead to improved corrosion resistance and mechanical properties in the joint [20−22].

Most reports in the literature are based on the effects of joining parameters on the microstructure and mechanical properties of the bond and bonding kinetics [23−27]. Studies focusing on the effects of standard heat treatment cycles on the diffusion brazed joints or a combination of diffusion brazing and standard heat treatment are still scarce. Moreover, the effect of full solution annealing and the subsequent heat treatments after diffusion brazing of IN-738LC superalloy on the microstructure and mechanical properties of the bond have been less studied to date. Therefore, the aim of the present research is set to study the influence of standard heat treatment of IN-738LC on the microstructure and mechanical properties of both isothermally solidified and non-isothermally solidified specimens. In addition, the main goal is to obtain an ideal joint with similar microstructure and mechanical properties as the substrate material.

2 Experimental

In this investigation, cast Ni-based superalloy IN-738LC was used as the substrate material. The chemical composition of the superalloy as determined using spark emission spectroscopy was: 15.10 Cr, 8.30 Co, 3.40 Al, 3.60 Ti, 2.70 W, 1.90 Mo, 1.70 Ta, 0.90 Nb, 0.11 C, 0.07 Fe, 0.04 Zr, 0.01 B, 0.01 Si (in wt.%) and balance Ni. BNi-9 alloy with the chemical composition of 15.20 Cr, 3.94 B (in wt.%) and balance Ni was chosen as the filler alloy. The filler metal with 38 μm in thickness was inserted between two pieces of substrate in the form of an amorphous foil. The melting range of the BNi-9 interlayer is 1048−1091 °C. Test specimens with dimensions of 10 mm × 10 mm × 5 mm were sectioned from the SM using an NC wire electro-discharge machine (EDM). The filler metal was cut to the dimensions of the substrate material. To eliminate the oxide layers on the mating surfaces of the specimens and reduce the roughness of the surfaces, the substrate material was polished using 800-grit SiC paper. Subsequently, the substrate material and filler metal were ultrasonically cleaned in an acetone bath for about 15 min prior to the joining process. A fixture made from CrNiMo heat resistant steel was used to fix the specimens during the bonding process.

Bonding was performed in a furnace under a vacuum of approximately 4.67×10^{-3} Pa for different bonding time (non-isothermal and isothermal solidification conditions) as presented in Table 1. The joints were then heat-treated for homogenization using three distinct and consecutive steps of standard IN-738LC heat treatment (SHT) namely full-solution, partial-solution and aging (1200 °C, 4 h, AC + 1120 °C, 2 h, AC + 845 °C, 24 h, AC [28]). The heat treatment scheme for each specimen is summarized

in Table 1.

The bonded specimens were sectioned perpendicular to the joint line using spark machining. Standard metallography techniques were used for specimen preparation. The bonded specimens were etched with a Marble solution (50 mL HCl, 50 mL H_2O and 10 g $CuSO_4$) for microstructure observations. The microstructural investigations were done using optical microscopy (OM), scanning electron microscope (SEM) and field emission scanning electron microscopy (FE-SEM). The chemical composition of the phases was determined using TESCAN MIRA3 FE-SEM equipped with an ultra-thin window energy dispersive X-ray spectrometer (EDS) for semi-quantitative analysis.

Hardness measurements were carried out using a Buehler Vickers microhardness machine with a 25 g load and a holding time of 15 s. Hardness mapping was done using the data obtained from the microhardness tester and OriginPro software to evaluate the hardness of the joints. It should be mentioned that 100 points for hardness were tested for each specimen. Shear tests were performed at room temperature as per ASTM D1002 [29] using a Zwick Z250 tensile machine. The cross-head speed of the tensile tester was set to be 1 mm/min. A photograph of the custom-made fixture utilized for shear testing is shown in Fig. 1. Three shear tests were done for each joint ID listed in Table 1. The edge effects were eliminated using EDM before carrying out the tests.

3 Results and discussion

3.1 Microstructure of substrate material

Figure 2 shows FE-SEM images of γ' precipitates before and after standard heat treatment of the substrate material. According to Fig. 2(a), before SHT, γ' precipitates are shapeless, tightly packed and also nonhomogeneous. This is due to the segregation of Ti and Al elements to regions close to the initial γ' precipitates during non-equilibrium casting. In this way, new γ' particles will form in these areas and stick to the initial γ' precipitates. Moreover, the growth of these particles is hindered due to lack of alloying elements near the newly formed γ' precipitates. That is why these particles become irregular shaped.

After SHT, the γ' precipitates are separate, block-shape and have an ordered structure (Fig. 2(b)). The reason for the block-shape can be attributed to the elastic strain energy associated with the formation of the second phase overpowering the interface energy between the matrix and precipitates, which leads to altering the

Table 1 Bonding and PBHT conditions of TLP specimens

Joint ID	Bonding temperature/°C	Bonding time/min	Post bond heat treatment (PBHT)
NHT-5	1120	5	–
NHT-45	1120	45	–
HT-5	1120	5	SHT (1200 °C, 4 h, AC + 1120 °C, 2 h, AC + 845 °C, 24 h, AC)
HT-45	1120	45	SHT (1200 °C, 4 h, AC + 1120 °C, 2 h, AC + 845 °C, 24 h, AC)

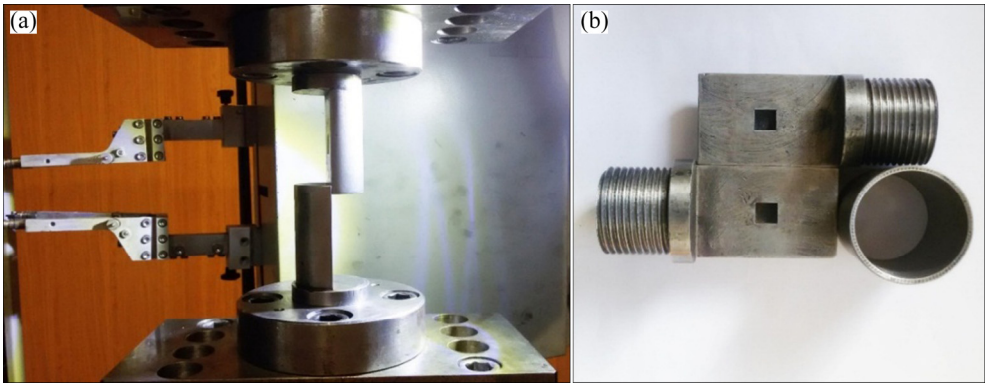

Fig. 1 Custom-made shear test fixture for exerting shear stress on joints

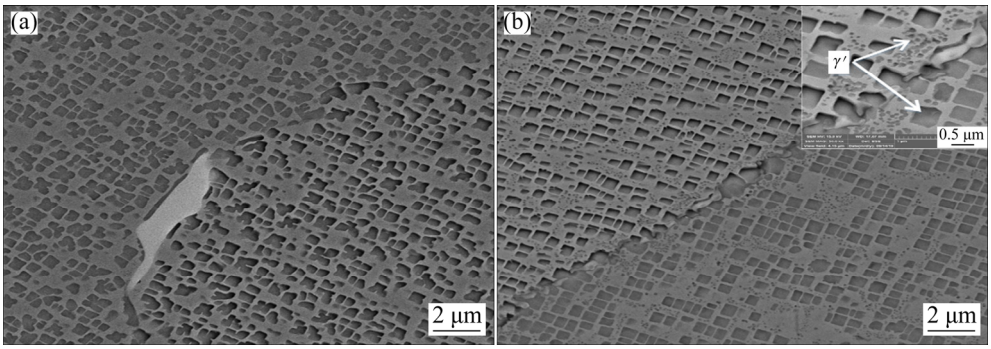

Fig. 2 FE-SEM images of γ' precipitates in IN-738LC substrate material: (a) Before SHT; (b) After SHT

shape of γ' particles from spherical to blocky [30]. Moreover, full solution annealing leads to the dissolution of γ' precipitates and creates uniform distribution of alloying elements in the surrounding γ matrix [28]. As a result, γ' precipitates do not adhere to each other.

Figure 3 shows the predicted amount of each equilibrium phase formed in the IN-738LC superalloy versus temperature computed using Thermo-Calc Software TTNI7 database. As seen in Fig. 3, the γ matrix is formed first with decreasing temperature from 1400 °C. This phase appears with an FCC crystal structure. The γ' particles precipitate in the γ matrix during further cooling to lower than 1200 °C. Carbides and TCP phases are formed as the temperature is decreased.

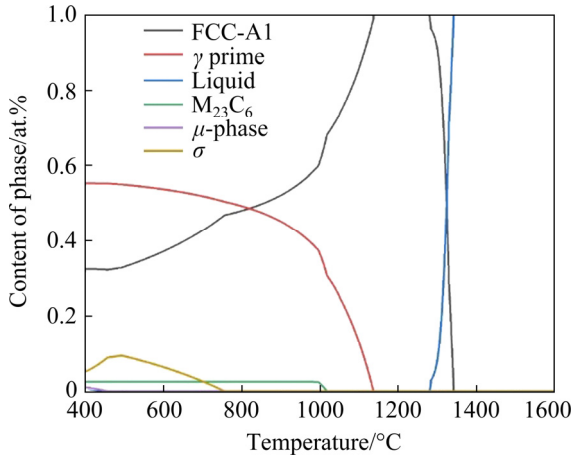

Fig. 3 Mole fractions of equilibrium phases as function of temperature for IN-738LC substrate material, computed using Thermo-Calc TTNI7 database

3.2 Microstructure of TLP joints

3.2.1 Samples of NHT-S and HT-S

The microstructure and chemical composition of various regions of the TLP bond joined at 1120 °C for 5 min (Sample NHT-5) are shown in Fig. 4(a) and Table 2, respectively. Figure 4(b) indicates the predicted amounts of equilibrium phases versus temperature in the BNi-9 filler metal. It should be mentioned that the values presented in Fig. 4(b) and Table 2 were computed using Thermo-Calc Software with TTNI7 database and the EDS results from the different phases. According to Fig. 4 and Table 2, the microstructure of the bond area for NHT-5 specimen is categorized into three zones.

(1) Isothermally solidified zone (ISZ)

This region consists of a nickel proeutectic solid-solution phase (γ). Under equilibrium condition, this zone is formed by inter-diffusion of boron from the molten interlayer to the substrate material during the temperature increase from liquidus to bonding temperature. Reports show that there is no segregation of boron at the liquid/solid interface in this zone [31]. As shown in Table 2, the composition of this zone is affected by the diffusion of alloying elements such as Ti, Al and Mo from the substrate material to the bond region.

(2) Athermally solidified zone (ASZ)

This area consists of nickel and chromium rich borides with eutectic-like morphology formed during non-isothermal solidification (Fig. 4(a) and Table 2). The formation of these phases is attributed to inadequate time for diffusion of boron from the interlayer to the substrate material during bonding process [32]. BAKHTIARI et al [33] showed that these borides form as Ni_4B_3, Cr_5B_3 and Cr_2B in the ASZ of diffusion brazed FSX-414 superalloy using BNi-9 filler metal. Figure 5 depicts the linear chemical concentration scan of the joints for all the bonded specimens. As can be seen from Fig. 5, there is a non-uniformity of the concentration of

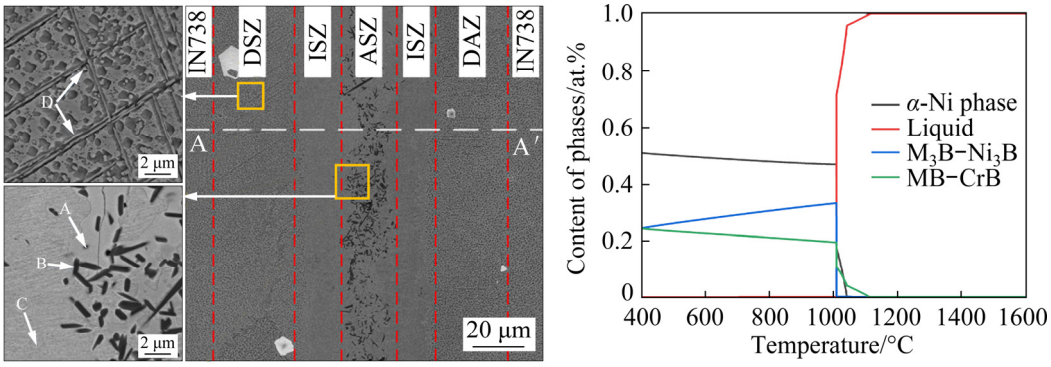

(a) (b)

Fig. 4 FE-SEM images of different regions in TLP joint of IN-738LC cast alloy using 38 μm BNi-9 interlayer carried out at 1120 °C for 5 min (a) and amount of equilibrium phases as function of temperature, calculated using EDS results and Thermo-Calc TTNI7 database in BNi-9 filler metal (b)

Table 2 FE-SEM/EDS analysis result of different areas specified in Fig. 4(a) (wt.%)

Region	Ni	Cr	Al	Ti	Co	Nb	Ta	W	Mo	Predicted phase
A	77.43	8.82	1.45	2.50	2.62	2.18	1.85	1.38	1.77	Ni_3B
B	19.00	69.95	1.11	0.84	1.27	1.61	0.98	2.77	2.47	CrB
C	73.90	15.07	1.55	1.18	2.38	1.29	1.06	1.70	1.87	γ
D	43.29	30.33	3.97	3.47	6.00	1.75	1.55	4.87	4.77	Cr−Mo−W rich boride

alloying elements in the center of joint area for NHT-5 specimen due to the formation of intermetallic phases.

(3) Diffusion affected zone (DAZ)

There are two distinguishable boride morphologies in this zone. Block-shaped and acicular-shaped borides are observed at the grains and grain boundaries of the substrate material. Table 2 shows that a high concentration of Cr, Mo and W is observed in these phases (Region D). Previous researchers have proven the existence of boron in these precipitates [34]. Therefore, it can be concluded that these precipitates are Cr−Mo−W rich borides. These borides are formed due to the high diffusion coefficient and low solubility of B in Ni (~0.3 wt.%) in the temperature range of 1060−1120 °C [35] and also, the high affinity of Cr, Mo and W elements for boron [36].

Figure 6 shows the OM and FE-SEM microstructures of the joint region in the HT-5 specimen joined at 1120 °C for 5 min after SHT. As can be observed from Fig. 6, the interface between the interlayer and substrate material is hardly indistinguishable. Performing full-solution annealing treatment on the non-isothermally solidified specimen led to a faint interface. Only a few spots at the center of the bond region show evidence of a previously liquid phase formed during SHT. This can be ascribed to the dissolution and re-melting of intermetallic phases in the ASZ (nickel and chromium rich borides) during full-solution annealing (1200 °C, 4 h) and presence of boron in the liquid phase. According to the Ni−B phase diagram [35], increasing the temperature to higher than the Ni−B eutectic temperature results in a decrease in the solubility of B in Ni, a decrease in the diffusion of B into the substrate material and additionally, aggregation of B in the remnant liquid phase. However, rejection of the substrate material alloying elements into the remnant liquid phase leads to the enrichment of the elements.

According to Fig. 4(b), nickel and chromium rich borides (depicted in the ASZ in Fig. 4(a)) have been dissolved at the solution annealing temperature. The amount of the molten phase is gradually decreased with the diffusion of B from the liquid phase into the γ matrix during solution annealing. The re-solidified products are formed from the remnant liquid after cooling from the solution annealing temperature (Fig. 6).

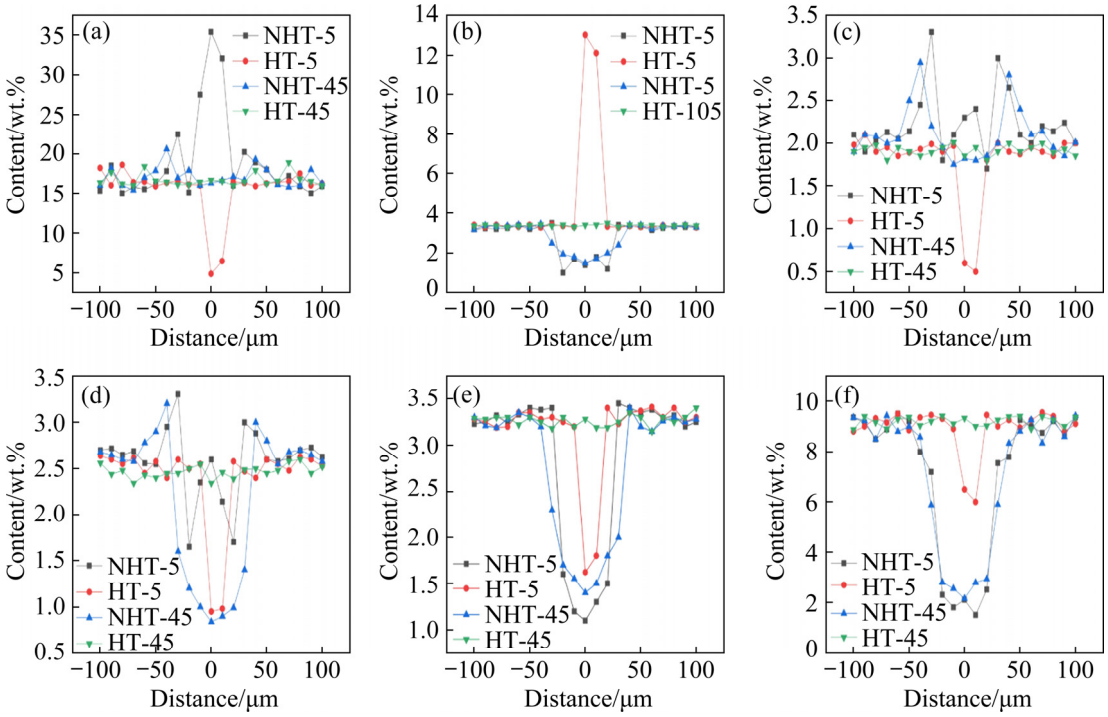

Fig. 5 EDS line scans of joints for specimens bonded using BNi-9 filler metal: (a) Cr; (b) Ti; (c) Mo; (d) W; (e) Al; (f) Co

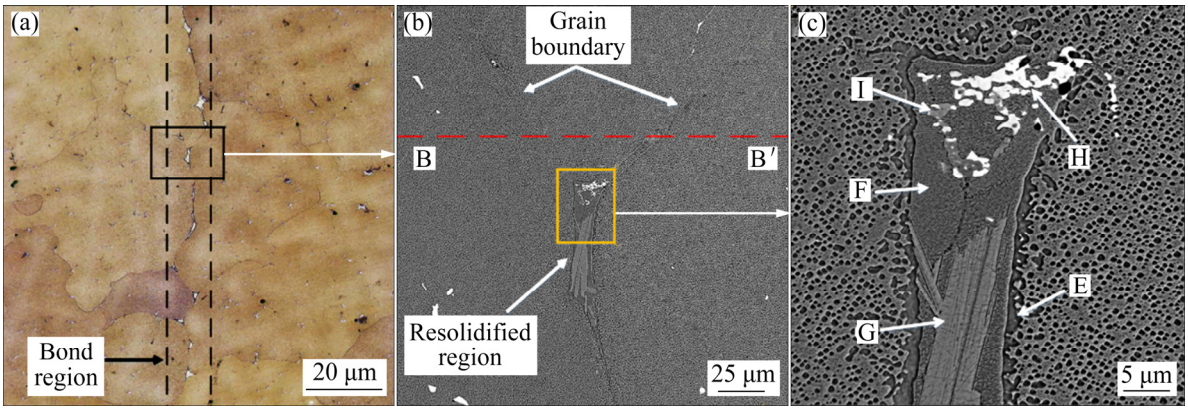

Fig. 6 Microstructure of bond region in HT-5 TLP joint specimen: (a) Optical micrograph; (b) FE-SEM microstructure; (c) Higher magnification of re-solidified products in joint

The chemical analysis of the regions shown in Fig. 6(c) for HT-5 specimen are presented in Table 3. The repartition map of alloying elements in the re-solidified zone for HT-5 specimen is illustrated in Fig. 7. The phases formed by the re-solidification of the remnant liquid phase during SHT process in the HT-5 specimen are: γ' precipitates, γ matrix, laminae of η phase, $M_{23}C_6$ carbides and Cr-, Mo- and W-rich carboborides.

There is a thick continuous film of γ' precipitates in Region E, as shown in Fig. 6(c). These precipitates are formed along the solid/liquid boundary. The elemental map (Figs. 7(d, e)) and Table 3 show the accumulation of Ti and Al in this region. The reason for the formation of these precipitates can be attributed to the segregation of γ' forming elements such as Ti and Al into the remaining liquid phase and the enrichment of the liquid of these elements. Moreover, according to Thermo-Calc software (Fig. 3), the γ' precipitates are formed during solidification from full-solution annealing temperature. It has been reported that the

Table 3 FE-SEM/EDS analysis result of various regions specified in Fig. 6(c) (wt.%)

Region	Ni	Cr	Al	Ti	Co	Nb	Ta	W	Mo	Predicted phase
E	69.36	5.25	3.44	9.51	4.54	0.75	5.82	0.42	0.91	γ'
F	56.76	17.69	1.98	4.50	9.63	0.87	3.61	2.35	2.61	γ
G	68.53	3.70	1.81	13.64	5.98	0.60	4.23	0.95	0.56	η
H	6.02	24.63	0.26	2.91	1.51	0.94	3.33	29.14	31.26	$M_{23}C_6$
I	26.42	42.39	0.94	2.84	3.81	0.68	1.70	8.87	12.35	Carboboride

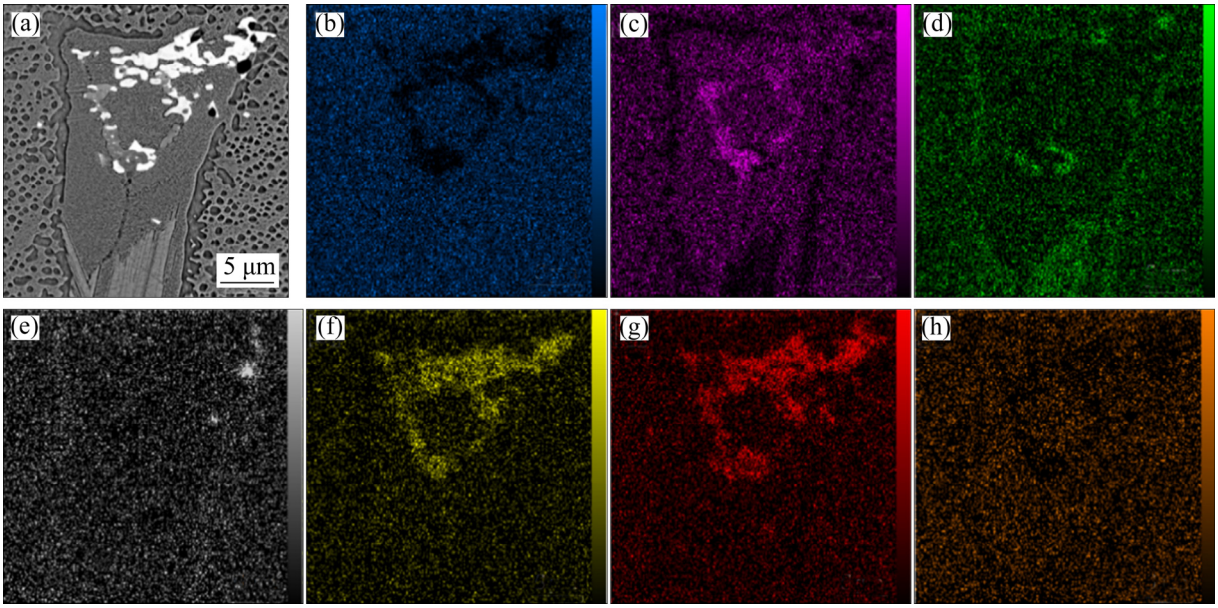

Fig. 7 FE-SEM image of re-solidified region in HT-5 sample (a) and element mapping analysis results: (b) Ni; (c) Cr; (d) Ti; (e) Al; (f) Mo; (g) W; (h) Co

existence of coarse and continuous γ' particles, such as those seen in this research, will result in a fragile structure and a reduction in mechanical properties [37].

EDS analysis from spot F in Fig. 6(c) (Table 3) shows the presence of the γ-nickel matrix. The presence of large amounts of chromium in this region represents the rejection of Cr into the remaining liquid phase during re-solidification.

The η phase with a laminar structure is shown in Fig. 6(c) (Region G). This phase is very fragile and does not have any adherence with the γ matrix. The laminar-shaped η phase (with a HCP crystal structure) is formed at the solution annealing temperature as a result of reaction of the cube-shaped γ' phase (with a FCC crystal structure) with alloying elements in the matrix. In other words, when the amount of Ti exceeds its solubility limit in Ni (2.7 at.%), the precipitation of the η phase (Ni_3Ti) will occur [38]. Table 3 and Fig. 7(d) confirm that the η phase is rich in titanium. CHOI et al [39] have shown that the deposition of sheet-shaped η phase at the grain boundaries will adversely affect the overall mechanical properties of the joint.

A high concentration of Cr, Mo and W in Region H of Fig. 6(c) (Table 3) and Figs. 7(c, f, g), confirms the existence of $M_{23}C_6$ carbides in this area. These carbides are formed during heat treatment cycles and also from the decomposition of MC carbides in the aging treatment. In other words, the decomposition of MC carbides will result in providing carbon to form $M_{23}C_6$ carbides [40].

According to Table 3 and Figs. 7(c, f, g), the high concentration of Cr, Mo and W in Region I of Fig. 6(c) confirms that this phase is a Cr-, Mo- and W-rich carboboride. It has been reported elsewhere that these carboborides are created in the form of a complex FCC structure following three criteria: (1) the existence of potent carbide and boride forming elements such as Cr, Mo and W, (2) the presence of carbon from decomposition of MC

carbides during SHT and (3) solid-state diffusion of boron into the γ matrix [41]. LVOV et al [42] have shown that heat treatment can lead to promoting the development of Cr-, Mo- and W-rich carboboride phases with continuous breakdown of MC carbides. The presence of these phases in very close proximity of $M_{23}C_6$ carbides in Fig. 6(c), proves this claim.

As can be seen from Fig. 5, there is a non-uniformity in the distribution of alloying elements at the centerline of the bond region for HT-5 specimen due to the existence of the solidified liquid phase.

3.2.2 Samples of NHT-45 and HT-5

Figure 8 presents representative FE-SEM images of the joint region after completion of isothermal solidification at 1120 °C for 45 min (NHT-45). As can be seen, bonding for this longer time has resulted in the elimination of the ASZ zone and detrimental intermetallic phases in this region and also development of a single-γ phase in the joint (Fig. 8(a)). As a matter of fact, the extension of boron diffusion from strictly the joint region into the substrate material leads to a distinguishable growth of the ISZ in this sample. Moreover, as shown in Fig. 8(b), γ' precipitates are formed in the bond region close to the joint/SM interface. The size of γ' precipitates drops with increasing distance from the joint/SM interface towards the joint centerline. The reason for this can be attributed to the increased concentration of γ' forming elements (especially Ti and Al) in the vicinity of the joint/SM interface. The increased amount of Ti and Al observed in Fig. 5 is the evidence for this claim. Moreover, these γ' precipitates are much smaller than the ones in the substrate material (Fig. 8(b)). This is due to insufficient temperature and time for effective diffusion of γ' forming elements from the substrate into the joint region and also lack of post-bond heat treatment process.

Although bonding for 45 min has led to the elimination of intermetallic phases in the joint centerline, unwanted boride precipitates are observed in the DAZ. These borides are formed due to their high stability at the bonding temperature (Fig. 4(b)).

Microstructure of Sample HT-45 joint is displayed in Figs. 9(a−c). According to Fig. 9, the microstructures of the bond and substrate material have completely blended together after SHT. EDS line scan of the bond region (Fig. 5) shows the similarity of the chemical composition across the joint and the substrate material in this sample. This seamless transition from the joint to the SM can be attributed to complete diffusion of alloying elements into the joint region. In addition, complete elimination of the boride precipitates in the DAZ during SHT (especially solution annealing) contributes to the observed uniformity. As can be seen in Figs. 2(b) and 9(c), the primary γ' precipitates are similar to those in the substrate material in terms of shape, density and size. According to Fig. 3, applying full solution annealing at 1200 °C has resulted in complete dissolution of γ' precipitates of the substrate material adjacent to the bond and the diffusion of their constituent elements especially Ti and Al into the joint region. Moreover, diffusion of Al and Ti in Sample HT-45 takes place in liquid ISZ (at full solution temperature) on the contrary to NHT-45 specimen where diffusion occurs in solid ISZ (at bonding temperature). Aging treatment has led to the formation of small and spherical secondary γ'

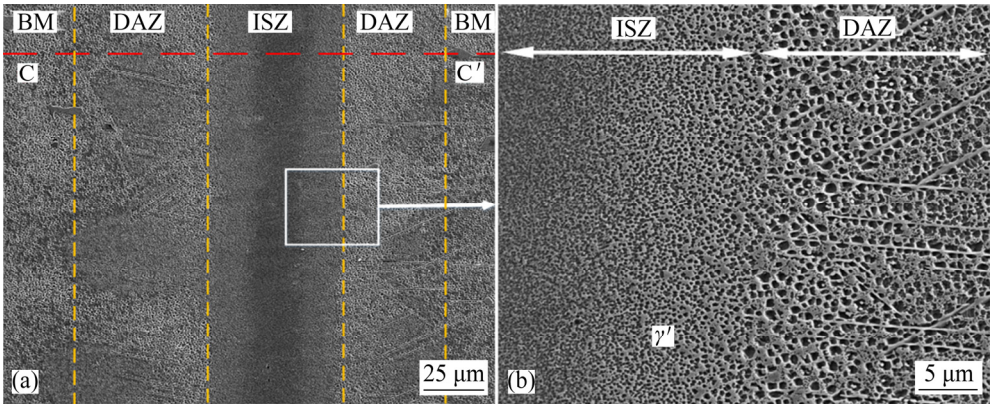

Fig. 8 FE-SEM images of joint region carried out at 1120 °C for 45 min (Sample NHT-45): (a) Bond region; (b) Higher magnification of joint/SM interface

precipitates in the bond region. In general, applying the SHT on Sample HT-45 results in the development of primary and secondary γ' precipitates in the joint with volume fraction, morphology, and size analogous to those in the substrate material (Fig. 9(c)).

3.3 Mechanical properties before and after PBHT

3.3.1 Microhardness

Hardness maps of NHT-5, NHT-45, HT-5 and HT-45 joints are presented in Fig. 10. It can be concurred that the center of the joint is very hard in NHT-5 compared to NHT-45. The average hardness at the center of the joint is 795 HV for NHT-5 and 315 HV for NHT-45 (Figs. 10(a, b)). This can be attributed to the presence of intermetallic phases (Cr and Ni rich borides) in the centerline of Sample NHT-5. Also, the DAZ hardness is much higher than that of the BM for both NHT-5 and NHT-45. This is because of the formation of borides in the substrate material close to the bond region. There is no noticeable difference between the DAZ hardness in the NHT-5 and NHT-45 (The average DAZ hardness is 623 and 592 HV for NHT-5 and NHT-45, respectively).

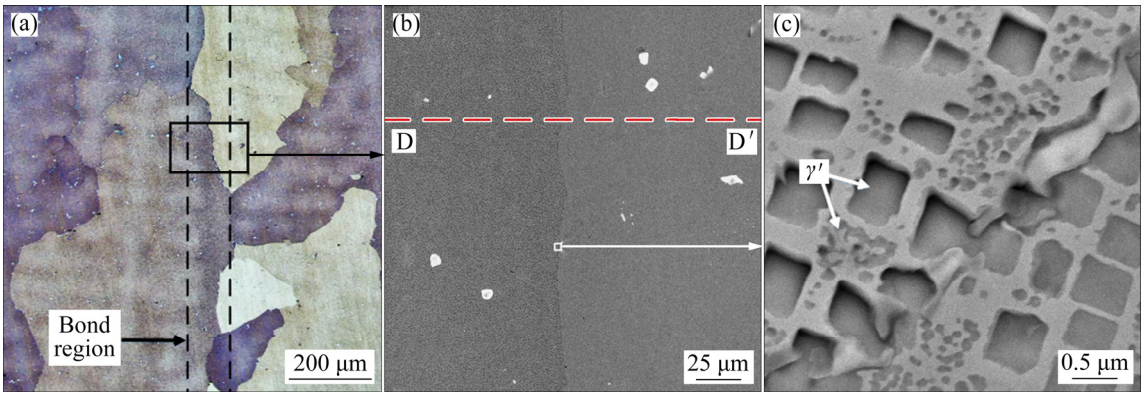

Fig. 9 Microstructure of bond region in Sample HT-45 TLP joint: (a) Optical micrograph; (b) FE-SEM image; (c) Higher magnification of joint

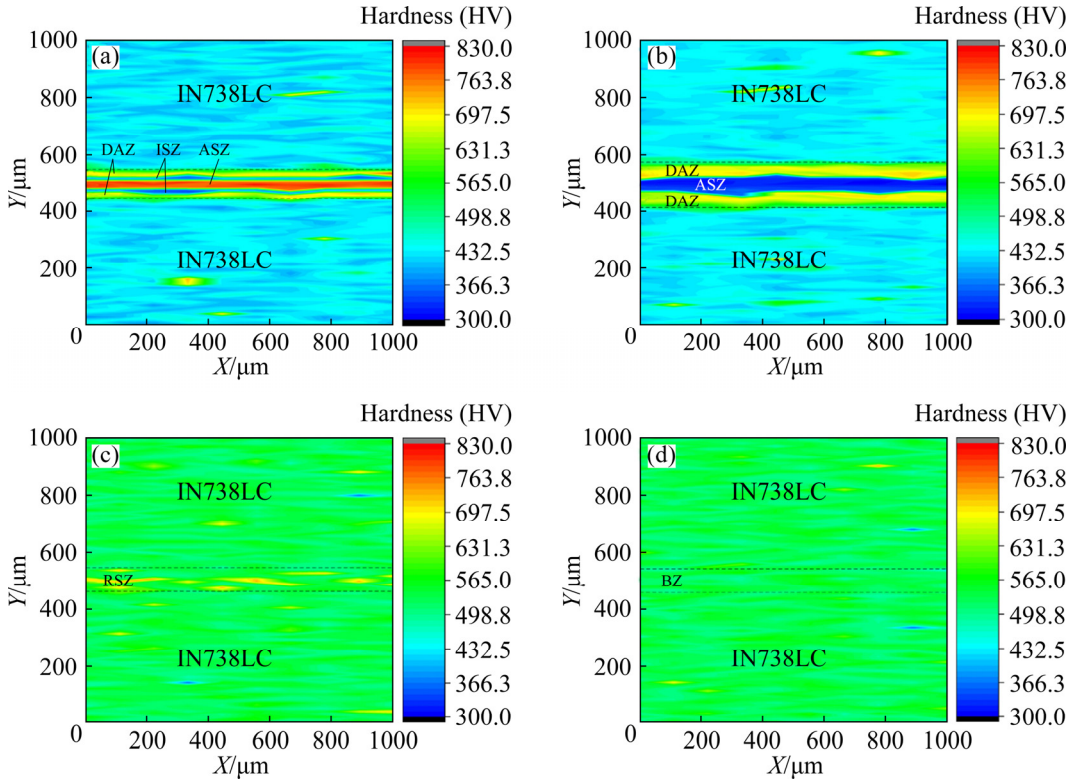

Fig. 10 Hardness maps of different samples: (a) NHT-5; (b) NHT-45; (c) HT-5; (d) HT-45

In Sample HT-5, although there is no hardness peak in the DAZ, an increase in hardness is observed in the center of the joint (Fig. 10(c)) due to the existence of brittle re-solidified products such as η phase laminae, $M_{23}C_6$ carbides and Cr-, Mo- and W-rich carboborides. Other regions in this specimen have analogous hardness values to the substrate material.

According to Fig. 10(d), there is an overall increase in hardness in Sample HT-45 compared to the NHT samples. The hardness map of HT-45 shows complete uniformity similar to the substrate material. This is because of the full dissolution of γ' particles in the substrate material during full-solution annealing at 1200 °C and the full diffusion of alloying elements, especially Ti and Al, into the joint region. Moreover, the formation of spherical secondary γ' precipitates during aging treatment is one of the reasons for the improvement of hardness in the bond region and substrate material. Additionally, the hardness peak observed in the DAZ of NHT-5 and NHT-45 samples is no longer present in HT-45 sample and the hardness of the joint is indistinguishable from the substrate material. This is due to the full dissolution of boride phases in this area during heat treatment at the high full-solution temperature.

3.3.2 Shear strength

Figure 11(a) displays load−displacement curves and Fig. 11(b) summarizes the maximum shear stress and toughness achieved from shear tests carried out on the joints before and after SHT and also BM after SHT. The area under the load−displacement curve for each of the joints is calculated as the toughness.

The shear strength of the IN738LC is measured to be ~811 MPa after SHT. Sample NHT-5 has the lowest shear strength compared to other joints and it is only 32% that of the substrate material. After the completion of isothermal solidification (Sample NHT-45), the shear strength of the joint increases to 74% that of the SM. According to Fig. 11, toughness and maximum displacement to failure are considerably improved in NHT-45 compared to NHT-5. This can be attributed to complete elimination of brittle intermetallic compounds in the NHT-45 joint.

Moreover, application of SHT to HT-5 and HT-45 samples leads to the improvement of shear strength, toughness and maximum displacement to failure. This is due to complete removal of DAZ precipitates and also the formation of the primary and secondary γ' precipitates in the joint district similar to the substrate material. However, Sample HT-45 shows greater performance than the HT-5 joint. For example, the shear strength of HT-5 and HT-45 is approximately 81% and 99% that of the substrate material, respectively. Additionally, the toughness of HT-45 joint (76.3 J) is higher than that of HT-5 joint (46.1 J). A similar comparison can be made for the maximum displacement to failure for the two joints. This is because of the brittle re-solidified phases formed during and after SHT process in the joint region of Sample HT-5.

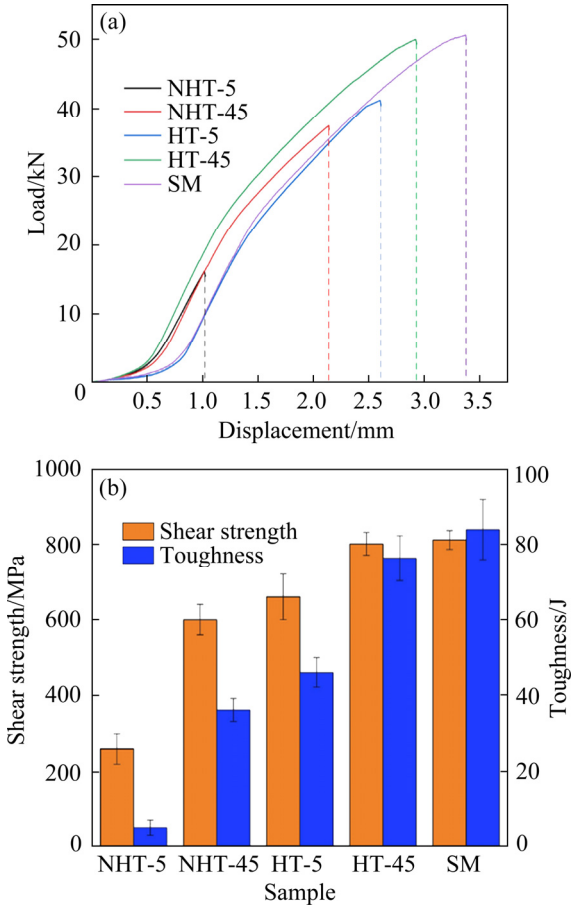

Fig. 11 Shear test results carried out on bonded specimens and SM: (a) Load–displacement curves; (b) Summary of shear strength and toughness

Generally speaking, applying the post heat treatment to Sample HT-45 means that there is no need for the SHT on the substrate material before joint/repair of segments. Additionally, an ideal joint analogous to the substrate material can be achieved without the need for any additional treatment (i.e. only TLP bonding and subsequent SHT of the

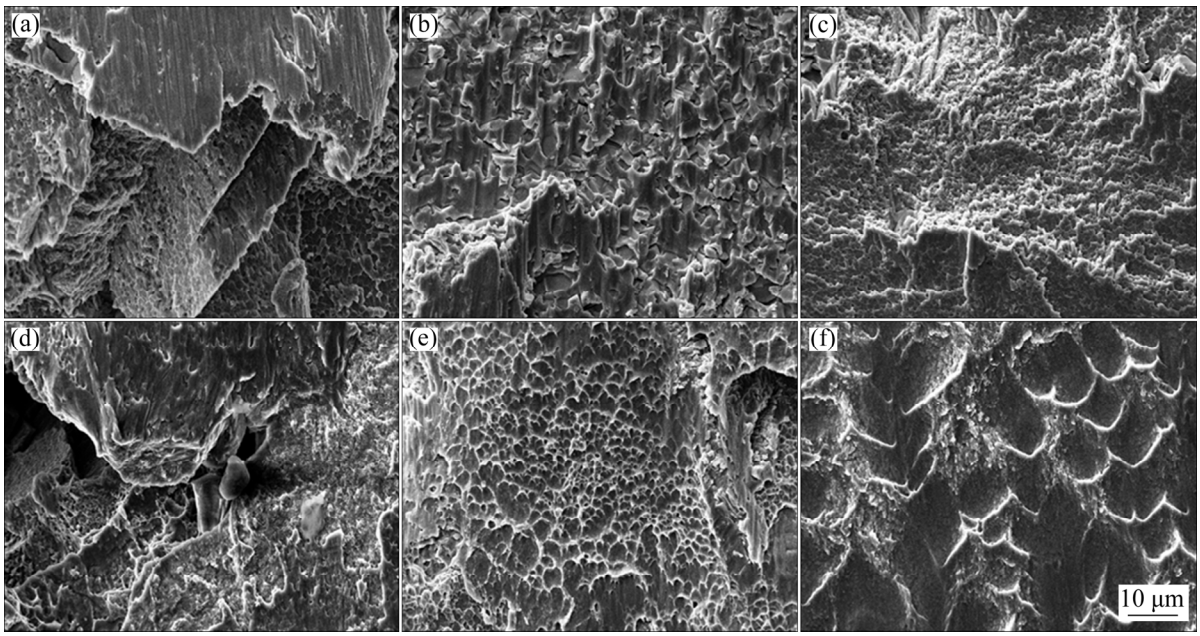

Fig. 12 SEM images of shear fracture surface: (a) NHT-5; (b, c) NHT-45; (d, e) HT-5; (f) HT-45

substrate material are required). This can drastically reduce the dedicated time and resources in relevant industrial applications.

Figure 12 displays the fracture surfaces of the joints before and after PBHT. As can be seen in Fig. 12(a), the fracture surface of Sample NHT-5 shows cleavage morphology. This corresponds to the presence of a brittle and continuous boride phase in the ASZ of this joint which is nominated as suitable sites to nucleate and propagate cracks. This is why the shear strength of this sample is the lowest amongst all the joints (Fig. 11(b)). The fracture morphology of the joint after complete isothermal solidification (Sample NHT-45) shows two types of surfaces also known as a cellular fracture surface [43]: (1) semi-cleavage facets and (2) shallow dimples (Figs. 12(b, c)). In the case of Sample NHT-45, the cellular fracture is related to the crack progressing through brittle and hard (Mo, Cr and W)-rich borides located in the elastic matrix in the DAZ of the substrate material. The fracture surface in this sample is in a mixture of brittle−ductile mode.

Performing PBHT on Sample HT-5 leads to a morphology containing both dimples and split particles after the shear test (Figs. 12(d, e)). The split particle structure further confirms the existence of brittle re-solidified products in the joint district. This mode of fracture corresponds to the lower shear strength observed in the HT-5 joint when compared to HT-45 joint. The fracture surface in Sample HT-45 consists of deep dimples showing a ductile fracture (Fig. 12(f)). This aligns well with the observed shear strength of this sample (Fig. 11(b)).

4 Conclusions

(1) A metastable eutectic structure is observed in the center of the joint after bonding at 1120 °C for 5 min due to the non-isothermal solidification of the filler metal.

(2) Solid-state diffusion of boron from the interlayer into the substrate leads to the precipitation of Cr-, Mo- and W-rich borides in block form and acicular-shape in the grains and at grain boundaries of the substrate.

(3) A distinct growth of the ISZ is observed in the specimen bonded at 1120 °C for 45 min due to the extension of boron diffusion from the joint region into the substrate. A non-uniformity of alloying elements is also observed in the joint district.

(4) Performing SHT on the non-isothermally solidified specimen leads to the complete elimination of boride phases in the DAZ and formation of γ' precipitates in the joint. Nevertheless, re-solidified products are observed in

some areas at the center of the bond region.

(5) The isothermally solidified joint after SHT shows very high similarities in terms of chemical composition, microstructure and also γ' precipitates.

(6) The sample with complete isothermal solidification and 45 min of SHT shows a completely uniform hardness in the joint region similar to the substrate material. Moreover, the highest shear strength and toughness of the joint are achieved in this sample.

Acknowledgments

The authors appreciate the support from Ferdowsi University of Mashhad (FUM) under the research scheme (No. 2/45210). The authors also acknowledge the technical assistance on Thermo-Calc Software calculations from the Canadian Centre for Welding and Joining (CCWJ) at University of Alberta.

References

[1] POLLOCK T M. Alloy design for aircraft engines [J]. Nature Materials, 2016, 15: 809−815.

[2] POLLOCK T M, TIN S. Nickel-based superalloys for advanced turbine engines: Chemistry, Microstructure, and Properties [J]. Journal of Propulsion and Power, 2006, 22: 361−374.

[3] CHEN Kai-cheng, CHEN Tai-cheng, SHIUE Ren-kae, TSAY Leu-wen. Liquation cracking in the heat-affected zone of IN738 superalloy weld [J]. Metals, 2018, 8: 387. https://doi.org/10.3390/met8060387.

[4] BANERJEE K, RICHARDS N L, CHATURVEDI M C. Effect of filler alloys on heat-affected zone cracking in preweld heat-treated IN-738 LC gas-tungsten-arc welds [J]. Metallurgical and Materials Transactions A, 2005, 36: 1881−1890. https://doi.org/10.1007/s11661-005-0051-1.

[5] AINA J O. A study of laser weldability of IN-738 nickel-based superalloy in a new pre-weld heat treatment condition [D]. Winnipeg: University of Manitoba, 2014.

[6] OJO O A, RICHARDS N L, CHATURVEDI M C. Microstructural study of weld fusion zone of TIG welded IN 738LC nickel-based superalloy [J]. Scripta Materialia, 2004, 51: 683−688. https://doi.org/10.1016/j.scriptamat.2004.06.013.

[7] OJO O A, RICHARDS N L, CHATURVED M C. Contribution of constitutional liquation of gamma prime precipitate to weld HAZ cracking of cast Inconel 738 superalloy [J]. Scripta Materialia, 2004, 50: 641−646.

[8] LIN W, LIPPOLD J C, BAESLACK W A. An investigation of heat-affected zone liquation cracking. Part 1 — A methodology for quantification [J]. Welding Journal, 1993, 71: 135s−153s.

[9] GHASEMI A, POURANVARI M. Microstructural evolution mechanism during brazing of Hastelloy X superalloy using Ni−Si−B filler metal [J]. Science and Technology of Welding and Joining, 2018, 23: 441−448. https://doi.org/10.1080/13621718.2017.1410341.

[10] RIGGS B B, ALEXANDROV B B, BENATAR A A, XU R R. Thermodynamic and kinetic simulations of high temperature brazing: Microstructure evolution in CMSX-4 joints [J]. Science and Technology of Welding and Joining, 2017, 22: 428−437. https://doi.org/10.1080/13621718.2016.1250432.

[11] DUVALL D S, OWCZARSKI W A, PAULONIS D F. TLP bonding: A new method for joining heat resistant alloys [J]. Weld J (NY), 1974, 53: 203−214.

[12] NAEIMIAN H, MOFID M A. TLP bonding of Ti−6Al−4V to Al 2024 using thermal spray Babbitt alloy interlayer [J]. Transactions of Nonferrous Metals Society of China, 2020, 30: 1267−1276. https://doi.org/10.1016/S1003-6326(20)65294-3.

[13] MALEKI V, OMIDVAR H, RAHIMIPOUR M. Effect of gap size on microstructure of transient liquid phase bonded IN-738LC superalloy [J]. Transactions of Nonferrous Metals Society of China, 2016, 26: 437–447. https://doi.org/10.1016/S1003-6326(16)64132-8.

[14] YUAN L, XIONG J T, DU Y J, REN J, SHI J M, LI J L. Microstructure and mechanical properties in the TLP joint of FeCoNiTiAl and Inconel 718 alloys using BNi_2 filler [J]. Journal of Materials Science and Technology, 2021, 61: 176–185. https://doi.org/10.1016/j.jmst.2020.05. 050.

[15] HADIBEYK S, BEIDOKHTI B, SAJJADI S A. Effect of bonding time and homogenization heat treatment on the microstructure and mechanical properties of the transient liquid phase bonded dissimilar GTD-111/FSX-414 TLP superalloys [J]. Journal of Alloys and Compounds, 2018, 731: 929−935. https://doi.org/10.1016/j.jallcom.2017.10.105.

[16] SHENG N C, LIU J D, JIN T, SUN X F, HU Z Q. Precipitation behaviors in the diffusion affected zone of TLP bonded single crystal superalloy joint [J]. Journal of Materials Science & Technology, 2015, 31: 129−134. https://doi.org/ 10.1016/j.jmst.2014.11.008.

[17] CHEN J, DEMERS V, TURNER D P, BOCHER P. Experimental investigation on high-cycle fatigue of Inconel 625 superalloy brazed joints [J]. Metallurgical and Materials Transactions A, 2018, 49: 1244−1253. https://doi.org/10.1007/s11661-018- 4474-x.

[18] POURANVARI M, EKRAMIK A, KOKABI A H. Microstructure evolution mechanism during post-bond heat treatment of transient liquid phase bonded wrought IN718 superalloy: An approach to fabricate boride-free joints [J]. Journal of Alloys and Compounds, 2017, 723: 84−91. https://doi.org/10.1016/j.jallcom.2017.06.206.

[19] WANG S Y, SUN Y, HOU X Y, CUI C Y, SUN X F, ZHOU Y Z. Investigation on microstructure and mechanical properties of a vacuum brazed joint of γ'-strengthened Co-based single crystal superalloy before and after the post-bond heat treatment [J]. Vacuum, 2020, 177: 109413. https://doi.org/10.1016/j.vacuum.2020.109413.

[20] WANG G L, SUN Y, WANG X G, LIU J D, LIU J L, LI J G, YU J J, ZHOU Y Z, JIN T, SUN X D, SUN X F. Microstructure evolution and mechanical behavior of Ni-based single crystal superalloy joint brazed with mixed

powder at elevated temperature [J]. Journal of Materials Science and Technology, 2017, 33: 1219−1226. https://doi.org/10.1016/j.jmst. 2017.01.027.

[21] MURRAY D C, CORBIN S F. Determining the kinetics of transient liquid phase bonding (TLPB) of Inconel 625/BNi-2 couples using differential scanning calorimetry [J]. Journal of Materials Processing Technology, 2017, 248: 92−102. https://doi.org/10.1016/j.jmatprotec.2017.05.013.

[22] WANG S Y, SUN Y, CUI C Y, SUN X F, ZHOU Y Z, MA Y M, AN H L. Effect of post-bond heat treatment on the microstructure and high temperature mechanical property of a TLP bonded γ'-strengthened Co-based single crystal superalloy [J]. Journal of Materials Science & Technology, 2020, 80: 244−258. https://doi.org/10.1016/j.jmst.2020.05.078.

[23] ARHAMI F, MIRSALEHI S E, SADEGHIAN A. Effect of bonding time on microstructure and mechanical properties of diffusion brazed IN-939 [J]. Journal of Materials Processing Technology, 2019, 265: 219−229. https://doi.org/10.1016/j.jmatprotec.2018.10.021.

[24] MACISAAC C, WHITMAN C A, CORBIN S F. Development of a boron-free filler metal for brazing nickel-based superalloys utilizing the Cu−Mn−Ni system [J]. Journal of Materials Science, 2020, 55: 8741−8755. https://doi.org/10.1007/s10853-020-04594-7.

[25] MALEKI V, OMIDVAR H, RAHIMIPOUR M R. Influences of gap size and cyclic-thermal-shock treatment on mechanical properties of TLP bonded IN-738LC superalloy [J]. Transactions of Nonferrous Metals Society of China, 2018, 28: 920−930. https://doi.org/10.1016/S1003-6326(18)64726-0.

[26] LIN T S, LI H X, HE P, YANG X, HUANG Y D, LI L, HAN L. Effect of bonding parameters on microstructures and properties during TLP bonding of Ni-based super alloy [J]. Transactions of Nonferrous Metals Society of China, 2012, 22: 2112−2117. https://doi.org/10.1016/S1003-6326(11)61436-2.

[27] KHAZAEI B A, ASGHARI G, BAKHTIARI R. TLP bonding of dissimilar FSX-414/IN738 system with MBF80 interlayer: Prediction of solid/liquid interface location [J]. Transactions of Nonferrous Metals Society of China, 2014, 24: 996−1003. https://doi.org/10.1016/S1003-6326(14)63154-X.

[28] SAJJADI S A, ZEBARJAD S M, GUTHRIE R I L, ISAC M. Microstructure evolution of high-performance Ni-base superalloy GTD-111 with heat treatment parameters [J]. Journal of Materials Processing Technology, 2006, 175: 376−381. https://doi.org/10.1016/j.jmatprotec.2005.04.021.

[29] ASTM Standard. D1002-10 standard test method for apparent shear strength of single-lap-joint adhesively bonded metal specimens by tension loading (metal-to-metal) [S]. ASTM International, 2010. https://doi.org/10.1520/D1002-10.on.

[30] BERAHMAND M, SAJJADI S A. Morphology evolution of γ' precipitates in GTD-111 Ni-based superalloy with heat treatment parameters [J]. International Journal of Materials Research, 2013, 104: 275−280.

[31] ARHAMI F, MIRSALEHI S E. The effect of heat treatment sequence on microstructure and mechanical properties of diffusion brazed IN-939 superalloy [J]. Journal of Materials Processing Technology, 2019, 266: 351−362. https://doi.org/10.1016/j.jmatprotec.2018.11.020.

[32] MALEKAN A, FARVIZI M, MIRSALEHI S E, SAITO N, NAKASHIMA K. Effect of bonding temperature on the microstructure and mechanical properties of Hastelloy X superalloy joints bonded with a Ni−Cr−B−Si−Fe interlayer [J]. Journal of Manufacturing Processes, 2019, 47: 129−140. https://doi.org/10.1016/j.jmapro.2019.09.030.

[33] BAKHTIARI R, EKRAMI A, KHAN T I. The effect of TLP bonding temperature on microstructural and mechanical property of joints made using FSX-414 superalloy [J]. Materials Science and Engineering A, 2012, 546: 291−300. https://doi.org/10.1016/j.msea.2012.03.073.

[34] AMIRI D, SAJJADI S A, BAKHTIARI R, KAMYABI-GOL A. The role of TLP process variables in improvement of microstructure and mechanical properties in TLP joints of GTD-111/Ni-Cr-Fe-B-Si/GTD-111 system [J]. Journal of Manufacturing Processes, 2018, 32: 644−655. https://doi.org/10.1016/j.jmapro.2018.03.036.

[35] TOKUNAGA T, NISHIO K, HASEBE M. Thermodynamic study of phase equilibria in the Ni−Si−B system [J]. Journal of Phase Equilibria, 2001, 22: 291−299. https://doi.org/10.1361/105497101770338798.

[36] ZHANG B Q, SHENG G M, JIAO Y J, GAO Z H, GONG X F, FAN H, ZHONG J. Precipitation and evolution of boride in diffusion affected zone of TLP joint of Mar-M247 superalloy [J]. Journal of Alloys and Compounds, 2017, 695: 3202−3210. https://doi.org/10.1016/j.jallcom. 2016.11.306.

[37] SMASHEY R W. Effect of long time, high stress exposures on the microstructure of Rene-80 alloy [C]//AIME Annual Meeting. Cleveland Oh, 1970.

[38] BOUSE G K. Eta (η) and platelet phases in investment cast superalloys [C]//Superalloys. Champion, Pennsylvania: The Minerals, Metals & Materials Society, 1996: 163−172.

[39] CHOI B G, KIM I S, KIM D H, SEO S M, JO C Y. ETA phase formation during thermal exposure and its effect on mechanical properties in Ni-base superalloy GTD 111 [C]// Superalloys 2004. The Minerals, Metals & Materials Society, 2004, 163−171.

[40] VOICE W E, FAULKNER R G. Carbide stability in NIMONIC 80A* alloy [J]. Metallurgical and Materials Transactions A, 1985, 16: 511−520.

[41] IDOWU O A, OJO O A, CHATURVEDI M C. Microstructural study of transient liquid phase bonded cast INCONEL 738LC superalloy [J]. Metallurgical and Materials Transactions A: Physical Metallurgy and Materials Science, 2006, 37: 2787−2796. https://doi.org/10.1007/BF02586111.

[42] LVOV G, LEVIT V I, KAUFMAN M J. Mechanism of primary MC carbide decomposition in Ni-base superalloys [J]. Metallurgical and Materials Transactions A, 2004, 35: 1669−1679.

[43] HULL D. Fractography: Observing, measuring and interpreting fracture surface topography [M]. Cambridge University Press, 1999.

标准热处理对采用 BNi-9 焊料的瞬时液相连接 IN-738LC 高温合金的影响

Danesh AMIRI, Ata KAMYABI-GOL, Seyed Abdolkarim SAJJADI

Department of Materials Science and Engineering, Engineering Faculty,
Ferdowsi University of Mashhad, Mashhad, Iran

摘　要：研究标准热处理对扩散焊 IN-738LC 高温合金显微组织和力学性能的影响。对连接样品进行全固溶退火、部分固溶退火和时效处理 3 个不同的热处理。结果表明，在 1120 °C 下焊接 5 min，会导致不完全等温凝固，在焊缝处形成富 Ni、Cr 的硼化物共晶相。当保温时间延长到 45 min 时，接头中发生完全等温凝固，形成镍的先共晶固溶体 γ 相。等温凝固和非等温凝固样品的标准热处理能完全消除扩散影响区的硼化物相，并在等温凝固区形成 γ′析出相。然而，在非等温凝固样品的接头区观察到不连续的再凝固产物。等温凝固样品经标准热处理后，剪切强度最高(约 801 MPa)，为基材剪切强度的 99%。

关键词：IN738LC；标准热处理；扩散焊；等温凝固；γ′析出相；力学性能

(Edited by Bing YANG)